Journal of Fluids and Structures 92 (2020) 102787

Contents lists available at ScienceDirect

Journal of Fluids and Structures

journal homepage: www.elsevier.com/locate/jfs

Fluid–structure interactions of single and dual wall-mounted 2D flexible filaments in a laminar boundary layer

Xiang Zhang, Guowei He, Xing Zhang *

The State Key Laboratory of Nonlinear Mechanics, Institute of Mechanics, Chinese Academy of Sciences, Beijing 100190, China
School of Engineering Science, University of Chinese Academy of Sciences, Beijing 100049, China

ARTICLE INFO

Article history:
Received 22 May 2019
Received in revised form 25 October 2019
Accepted 29 October 2019
Available online xxxx

Keywords:
Fluid–structure interaction
Flow-induced oscillation
Frequency lock-in
Vortex shedding
Immersed boundary method

ABSTRACT

We numerically investigated the interactions of a laminar boundary layer flow with both single and dual wall-mounted 2D flexible filaments. The influences of various parameters, including bending rigidity, mass ratio, Reynolds number and interspace between two filaments, on the dynamics of the systems were explored systematically. Different modes of dynamic behavior in the single-filament and dual-filament systems were identified. The wake structures associated with different modes of dynamic behavior were compared. The physical mechanisms underlying the frequency lock-in phenomena observed in the flow-induced oscillations were also elucidated.

1. Introduction

Interactions between wall-mounted flexible structures and a transverse flow are widely seen in nature and engineering. For example, such interactions can be found in terrestrial and aquatic plants (Py et al., 2006; De Langre, 2008; Gosselin et al., 2010; Luhar and Nepf, 2011; Nepf, 2012; Gosselin, 2019; Huai et al., 2019), bio-inspired structures designed for flow control (Pinelli et al., 2016), energy harvesting (Nové-Josserand et al., 2018), and flow sensing (Tao and Yu, 2012). The research in this area is not only of fundamental importance in fluid mechanics, but is also potentially applicable to a wide variety of disciplines. Understanding the physical mechanisms that underlie the fluid–structure interaction (FSI) process is among the most challenging tasks in multiphysics analysis. In the past, substantial efforts have been put on flexible structures exposed to a spatially *uniform* flow (either axial or transverse) and abundant literature can be found in this area. The stability and flapping dynamics of a single filament facing an axial flow, clamped at either the leading edge (Zhang et al., 2002; Zhu and Peskin, 2002; Shelley et al., 2005; Huang et al., 2007; Connell and Yue, 2007; Alben and Shelley, 2008) or the trailing edge (Kim et al., 2013; Ryu et al., 2015; Shoele and Mittal, 2016; Sader et al., 2016) have been extensively studied. The coupling dynamics of multiple filaments in tandem and side-by-side arrangements (while facing an axial flow) were also studied (Zhu and Peskin, 2003; Ristroph and Zhang, 2008; Zhu, 2009; Kim et al., 2010; Tian et al., 2011; Uddin et al., 2013; Huang et al., 2017; Ryu et al., 2018). In the case of a transverse incoming flow, the static reconfiguration in a steady flow and the dynamic reconfiguration in a steady or an oscillatory flow (Alben et al., 2002; Zhu, 2007; Yang and Liu, 2016; Leclercq and De Langre, 2018; Leclercq et al., 2018) have been explored. For a more comprehensive literature review, please refer to Shelley and Zhang (2011) and Yu et al. (2019).

* Corresponding author at: The State Key Laboratory of Nonlinear Mechanics, Institute of Mechanics, Chinese Academy of Sciences, Beijing 100190, China.
E-mail address: zhangx@lnm.imech.ac.cn (X. Zhang).

https://doi.org/10.1016/j.jfluidstructs.2019.102787
0889-9746/

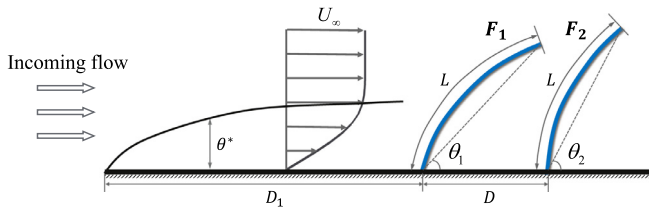

Fig. 1. A schematic diagram of the model problem. F_1 and F_2 denote the two filaments in the dual-filament system. L is the length of each filament. D_1 is the distance from the entrance to the first filament. D is the interspace between the two filaments. θ_1 and θ_2 represent the inclination angles of the chord lines (connecting the tip and the root) with the horizontal, for the two filaments, respectively. U_∞ denotes the velocity of the free stream. θ^* denotes the momentum thickness of the boundary layer.

In comparison with the FSI in open space, the FSI of wall-mounted flexible structures involves two additional complexities. First, the structures are actually exposed to a nonuniform incoming flow due to the existence of a boundary layer. Second, the solid boundary also causes some hindrances to the motion of the structures (through direct contact or flow-mediated interaction). The literature on this research topic is quite limited. The influence of a sheared incoming flow on the reconfiguration of a flexible plate have been explored by Henriquez and Barrero-Gil (2014) and later by Leclercq and De Langre (2016). In both works, a theoretical model with a prescribed nonuniform velocity profile was used to calculate the fluid load on the structure. The interaction of a wall-mounted structure with a turbulent flow was studied experimentally by Jin et al. (2018a,b, 2019). They focused on the influences of turbulent wake fluctuations, tip geometric shapes and inclined incoming flows on the dynamic behaviors of the structure. The coupling dynamics of two tandem wall-mounted flexible structures facing a turbulent flow were also studied by Jin et al. (2018c). It was found that the dynamics of the upstream structure was dominated by the vibration at its first natural frequency, whereas the dynamics of the downstream one were significantly modulated. Recently, some numerical simulations were also conducted to study the interaction between an array of wall-mounted flexible filaments and a unidirectional channel flow (Poiseuille flow) or an oscillating channel flow (Womersley flow) (O'Connor et al., 2016; Favier et al., 2017; O'Connor and Revell, 2019).

Despite of the useful insight gained in these studies, the understanding of the FSI mechanisms involving wall-mounted flexible structures is still far from complete. For example, the FSI of such structures in a laminar boundary layer is important to some applications (such as the design of bio-inspired flow sensors), but the systematic studies are still lacking. Under such circumstances, a significant part of the structure is immersed in a thick layer of sheared flow. Thus, there exists a tight two-way coupling between the boundary layer flow and the dynamics of the flexible structures. This is in contrast to the situations considered by Jin et al. (2018a,b, 2019, 2018c), where a very thin boundary layer in the Reynolds number range of $10^4 - 10^5$ was supposed to have a negligible impact on the dynamics of the structures.

Motivated by the previous works on FSI of wall-mounted structures, we use high-fidelity numerical simulations to investigate the flow-induced oscillations of such structures in a laminar boundary layer. Our emphases are placed on the dynamic behaviors of a single 2D flexible filament and the couple dynamics of two tandem 2D flexible filaments. The arrangement of the rest of the paper is as follows. The model problem is described in Section 2. The numerical methods and settings are introduced in Section 3. The results are discussed in Section 4. Some conclusions are drawn in Section 5.

2. Model description

We consider single and dual wall-mounted 2D flexible filaments which interact with a 2D laminar boundary layer flow. The schematic representation of the model is shown in Fig. 1. The filaments are of length L. The incoming flow is from left to right and has a uniform velocity at the left entrance. The distance from the entrance to the leftest filament is set to $15L$. For the dual-filament system, the interspace between the two filaments is D.

The fluid flow is governed by the incompressible Navier–Stokes equations, which can be written in a dimensionless form as

$$\frac{\partial \boldsymbol{u}}{\partial t} + (\boldsymbol{u}\cdot\nabla)\boldsymbol{u} = -\nabla p + \frac{1}{Re}\nabla^2\boldsymbol{u} + \boldsymbol{f}, \tag{1a}$$

$$\nabla\cdot\boldsymbol{u} = 0, \tag{1b}$$

where $\boldsymbol{u}$ and p are the velocity and pressure, respectively, $\boldsymbol{f}$ is the force which represents the effect of immersed bodies on the flow, and Re is the Reynolds number.

The governing equations for the motions of the flexible filaments can be written in a dimensionless form as

$$\beta\frac{\partial^2\boldsymbol{X}}{\partial t^2} - \frac{\partial}{\partial s}(\zeta\frac{\partial\boldsymbol{X}}{\partial s}) + \frac{\partial^2}{\partial^2 s}(\gamma\frac{\partial^2\boldsymbol{X}}{\partial s^2}) = -\boldsymbol{F} + \boldsymbol{F_c}, \tag{2a}$$

$$\frac{\partial\boldsymbol{X}}{\partial s}\cdot\frac{\partial\boldsymbol{X}}{\partial s} = 1, \tag{2b}$$

where $\boldsymbol{X}$ is the position vector of a Lagrangian point on the filament and s is the Lagrangian coordinate along the arc. $\boldsymbol{F}$ is the Lagrangian forcing that represents the interaction between the structure and the flow. The three dimensionless quantities that appear in Eq. (2a) are: mass ratio β, dimensionless tension ζ, and dimensionless rigidity γ. Here we only consider the situation in which the fluid load exerted on the structure is the dominant one. Thus, the influences of gravity and buoyancy force are disregarded.

The dimensionless equations in Eq. (1) and Eq. (2) are obtained by scaling the governing equations for the fluid flow and structure motion, by using L and LU_∞^{-1} as the reference length and reference time, respectively. The definitions of the four dimensionless quantities in Eq. (1) and Eq. (2) are:

$$Re = \frac{U_\infty L}{\nu}, \quad \beta = \frac{\rho_s \delta}{\rho_f L}, \quad \zeta = \frac{T}{\rho_f U_\infty^2 L}, \quad \gamma = \frac{B}{\rho_f U_\infty^2 L^3}, \tag{3}$$

where ν is the kinematic viscosity, ρ_f and ρ_s are the densities of the fluid and the structure, respectively. δ, T and B are the thickness, tension and bending rigidity of the structure, respectively. Please note that the dimensionless rigidity γ is actually the inverse of Cauchy number, which has been widely used in some previous studies (De Langre, 2008; Gosselin et al., 2010; Luhar and Nepf, 2011; Gosselin, 2019).

The model for the structure (Eq. (2)) is different from the classic or generalized nonlinear Euler–Bernoulli models that are widely used in the literature. This model was first proposed by researchers at the Courant Institute of Mathematical Sciences, New York University (Peskin and McQueen, 1993; Zhu and Peskin, 2002; Shelley and Zhang, 2011), and later extensively used by other groups (Huang et al., 2007; Connell and Yue, 2007; Zhu et al., 2014b; Favier et al., 2017). The geometric nonlinearity in this model is introduced by the inhomogeneous tension, which is also the Lagrange multiplier that enforces the inextensibility condition (Eq. (2b)) (Shelley and Zhang, 2011). The inhomogeneous tension can be determined by solving a linear boundary value problem, in which the governing equation for ζ is derived by rearranging Eq. (2a) and Eq. (2b) (Huang et al., 2007; Belmonte et al., 2001).

On the right-hand side of Eq. (2a), $\boldsymbol{F_c}$ is the short-range repulsive force that is added to avoid the tip-wall collision. The repulsive force is computed by using the formula proposed by Huang et al. (2007):

$$\boldsymbol{F_c}(s,t) = c_0 \cdot \beta \cdot \delta_h(\boldsymbol{X}(s,t) - \boldsymbol{X}'(s,t))\boldsymbol{j}, \quad (0.1 \le s \le 1) \tag{4}$$

where $\boldsymbol{X}'$ is the position vector of a point which is the projection of the Lagrangian point at $\boldsymbol{X}$ on the wall. $\boldsymbol{j}$ is the unit vector in the positive y-direction. δ_h is the three-point discrete delta function (Wang and Zhang, 2011). c_0 is an adjustable constant. The value of this constant is determined such that minimal repulsive force is applied to prevent the tip from penetrating into the wall. Through numerical experiments, it is found that $c_0 = 1.0$ can yield satisfactory results by avoiding direct contact and keeping the tip at least one grid width away from the wall. We also notice that the smallest gap distance is insensitive to the value of c_0, in the range of $1.0 \le c_0 \le 10.0$. The range of $s \in [0.1, 1.0]$ specified in Eq. (4) ensures that no repulsive force is applied to the Lagrangian points near the root.

3. Numerical methods and settings

3.1. Fluid and structure solvers

The fluid equations are solved by using the direct-forcing immersed boundary method based on the discrete stream-function formulation (Wang and Zhang, 2011; Wang et al., 2013). The structural equations are solved by using the numerical method proposed by Huang et al. (2007). The finite difference method is used for the spatial discretization. A three-time-level scheme is used for the temporal advancement, in which the tension term is treated explicitly while the bending term is treated implicitly. The FSI simulations are performed by loosely coupling the two different solvers, i.e., sequentially advancing the fluid equations and structure equations. This FSI code has been thoroughly validated and used in our previous studies on the free-swimming of a fish-like elastic filament (Zhu et al., 2014a,b; Dai et al., 2016, 2018a,b).

3.2. Numerical settings

The computational domain is a rectangular box of $[0, 32L] \times [0, 8L]$. On the left boundary, a uniform velocity is prescribed. On the right boundary, the outflow condition is implemented. The non-slip condition is imposed on the bottom boundary while the slip-wall condition is prescribed on the top boundary. On the filaments, the non-slip condition is enforced by using the direct-forcing immersed boundary technique (Wang and Zhang, 2011). Initially, the velocity of the fluid is set to U_∞, and all filaments stand upright and have zero velocity.

The boundary conditions for the wall-mounted flexible filaments are described as follows. At the fixed end (or root), the filament is vertically orientated and the boundary conditions are:

$$\boldsymbol{X} = (x_0, 0)^T, \quad \frac{\partial \boldsymbol{X}}{\partial s} = (0, 1)^T. \tag{5}$$

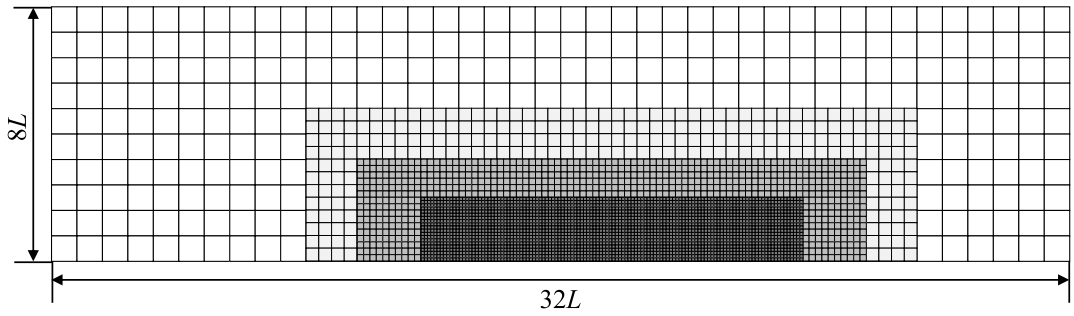

Fig. 2. Computational domain and multi-block Cartesian mesh used in the simulation. Please note that this is a schematic diagram in which the grid widths are not drawn to scale.

Table 1
Values of control parameters used in the present study.

$n^{\dagger}$	γ	β	Re	d
1	$10^{-4} \sim 10^{1}$	$0.01 \sim 10$	$50 \sim 800$	–
2	$10^{-4} \sim 10^{1}$	1.0	400	$0.5 \sim 8.0$

$^{\dagger}n$ denotes the number of filaments.

At the free end (or tip), the boundary conditions are:

$$\frac{\partial^2 \boldsymbol{X}}{\partial s^2} = (0,0)^T, \quad \frac{\partial^3 \boldsymbol{X}}{\partial s^3} = (0,0)^T. \tag{6}$$

A multi-block Cartesian mesh is generated for the simulation (see Fig. 2). The grid width ranges from $0.02L$ to $0.08L$ in the regions that are far away from the filaments. In the vicinity of the filaments (a rectangular domain of $[14L, 26L] \times [0, 2L]$), the grid width is reduced to $0.01L$ for capturing the vortical structure in the near wake region. The grid width for the spatial discretization of the structure equations is $0.01L$, which is the same as that for discretizing the N-S equations. The dimensionless time step used in the simulation is 0.002. At this time step size, the maximum Courant–Friedrichs–Lewy (CFL) number never exceeds 0.1. The ratio of the time step to the typical period of structure vibration lies in the range of 3×10^{-4}—8×10^{-4}. Thus, this time step is also sufficiently small for resolving the oscillating motions of the structure.

To ensure that the mesh resolution is sufficient for resolving the boundary layer flow, the velocity profiles at different distances from the entrance are compared with the Blasius solution. Moreover, tests are also conducted to ensure that solutions obtained are (almost) independent of the grid width, the time step size and the domain size. The details of the aforementioned validations and tests are presented in Appendix.

3.3. Parameter space

There are four dimensionless control parameters in the system: mass ratio β, dimensionless rigidity γ, Reynolds number Re, and dimensionless interspace $d = D/L$ (only for the dual-filament system). The values of these control parameters used in the present study are summarized in Table 1.

Based on the Blasius solution for a laminar flow past a flat plate, the momentum thickness of the boundary layer at the distance x from the leading edge (left entrance) can be computed by

$$\bar{\theta}^* = \frac{0.664\bar{x}}{\sqrt{Re_x}}, \tag{7}$$

where Re_x represents the Reynolds number based on the distance from the entrance, and the variables with a bar over them denote the dimensionless ones scaled by L. According to the values of control parameters listed in Table 1, the momentum thickness at the position of the leftest filament (i.e., $\bar{x} = 15$) lies in the range of 0.1 to 0.36. This implies that for all cases considered here, a significant part of the filament is immersed in the boundary layer.

4. Results and discussion

The inclination angle of the chord line (the straight line connecting the tip and root of the filament) with respect to the horizontal direction is the key quantity that is used for describing the dynamics of the system (see Fig. 1). More

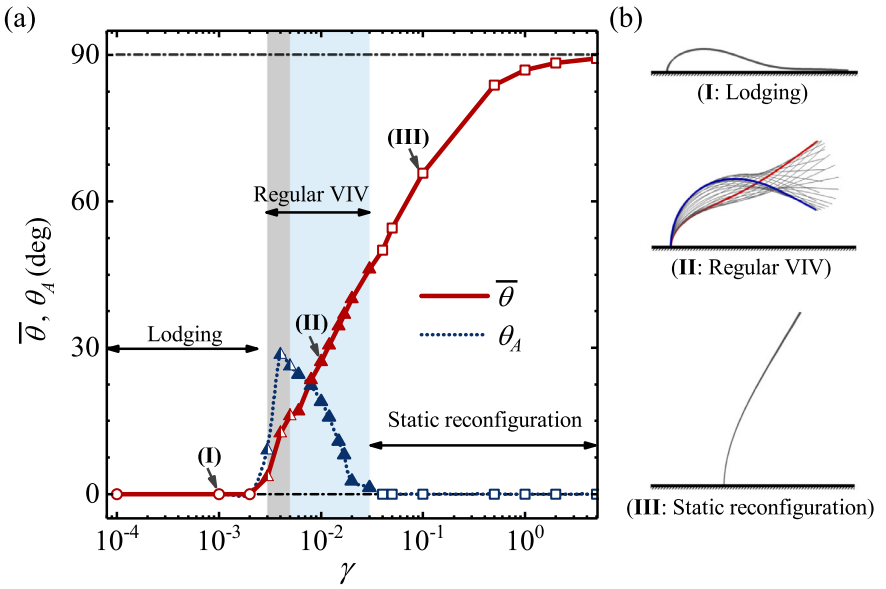

Fig. 3. Dynamic behaviors of the single-filament system at different bending rigidities. (a) Mean inclination angle $\bar{\theta}$ and amplitude of angular oscillation θ_A as a function of γ. (b) Amplitude envelops corresponding to the lodging ($\gamma = 0.001$), regular VIV ($\gamma = 0.01$) and static reconfiguration ($\gamma = 0.1$) modes. The fixed control parameters are: $\beta = 1.0$, $Re = 400$. The circles, triangles and squares denote the lodging, regular VIV and static reconfiguration modes, respectively. Within the regime of regular VIV mode, the semi-hollow and solid symbols represent the quasi-periodic and periodic oscillations, respectively.

specifically speaking, we use the mean inclination angle ($\bar{\theta}$) and the amplitude of angular oscillation (θ_A) to characterize the dynamic behaviors. The definitions of these two quantities are:

$$\bar{\theta} = \frac{1}{t_1 - t_0} \int_{t_0}^{t_1} \theta(t) dt, \tag{8a}$$

$$\theta_A = \{\max[\theta(t)] - \min[\theta(t)]\}|_{t_0 \le t \le t_1}, \tag{8b}$$

where the starting time t_0 is chosen such that the laminar boundary layer is fully developed and the periodicity in the oscillations of the filaments is also fully established. The time interval $(t_1 - t_0)$ is chosen to be 30, for the cases of periodic oscillation or static deformation. For the cases of quasi-periodic oscillation, the time interval is set to 100.

4.1. Single-filament system

4.1.1. Influences of bending rigidity, mass ratio and Reynolds number

The influences of three dimensionless parameters, i.e., γ, β and Re on the dynamic behaviors are studied by only varying one parameter while keeping the other two fixed.

We first explore the influence of rigidity on the dynamic behaviors. The mean inclination angle and the amplitude of angular oscillation are plotted as a function of γ and shown in Fig. 3, for $Re = 400$ and $\beta = 1.0$. From this figure, three distinct modes of dynamic behavior, namely, lodging, regular vortex-induced vibration (VIV) and static reconfiguration, can be identified. At low bending rigidity ($\gamma < 3\times10^{-3}$), the lodging mode, in which the filament falls flat on the ground, is exhibited. At intermediate bending rigidity ($3\times10^{-3} \le \gamma \le 3\times10^{-2}$), the regular VIV mode, in which sustained oscillation is superimposed on the static deformation, emerges. In this mode, the mean inclination angle increases monotonically with increasing rigidity. The amplitude of angular oscillation reaches the peak value of 30° at $\gamma = 0.004$ and then decreases with increasing rigidity. At large bending rigidity ($\gamma > 3 \times 10^{-2}$), the static reconfiguration mode is observed. The trend of the variation of mean inclination angle with increasing bending rigidity is the same as that in the regular VIV mode, while the amplitude of angular oscillation reduces to zero.

For the regular VIV mode, the flow-induced oscillation can be further categorized into quasi-periodic ($3 \times 10^{-3} \le \gamma \le 5 \times 10^{-3}$) and periodic ($5 \times 10^{-3} < \gamma \le 3 \times 10^{-2}$) sub-types. The difference between these two sub-types of oscillation can be clearly seen in Fig. 4, in which the time history of θ, the phase diagram spanned by the instantaneous inclination angle and angular velocity, and the normalized power spectra are shown. In the periodic sub-type, the angular oscillation is slaved to a singular frequency, while multiple frequencies are observed in the quasi-periodic sub-type. The frequency selection mechanism in the periodic oscillation will be addressed in Section 4.1.2. Since the rigidity range for

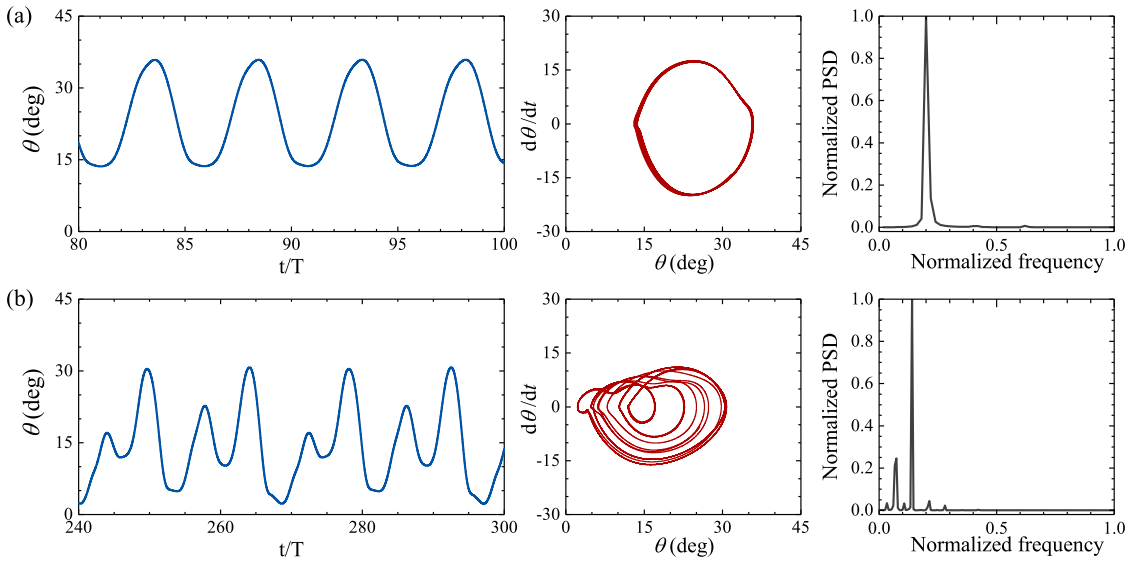

Fig. 4. Time histories of the inclination angle, the phase diagram (angular velocity vs. inclination angle), and the normalized power spectra of angular oscillations for the selected cases of (a) periodic oscillation ($\gamma = 0.008$) and (b) quasi-periodic oscillation ($\gamma = 0.004$). The fixed control parameters are: $\beta = 1.0$, $Re = 400$.

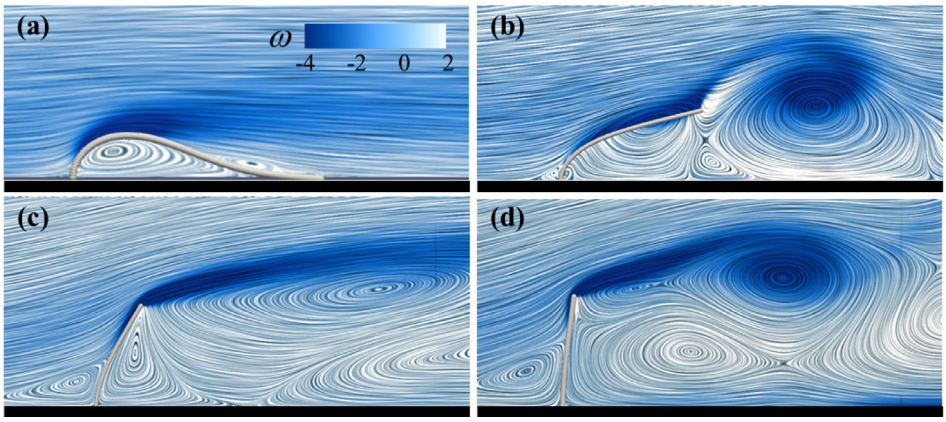

Fig. 5. Representative wake structures of the single flexible filament with different rigidity: (a) $\gamma = 0.001$, (b) $\gamma = 0.01$, (c) $\gamma = 0.1$, (d) $\gamma = 0.5$. The other control parameters are $\beta = 1.0$ and $Re = 400$. The contours of dimensionless vorticity and the streamlines are used to visualize the wake structures. In (a), (b) and (d), one snapshot of the unsteady flow is displayed; while in (c), the steady state is displayed.

the quasi-periodic sub-type is much narrower than that for the periodic sub-type, we believe that the quasi-periodic oscillation is a transitional state in between lodging and periodic oscillation states.

The wake structures corresponding to different bending rigidities are shown in Fig. 5. At $\gamma = 0.001$ (lodging mode), the free end (almost) attaches the wall and a enclosed region bounded by the filament and the wall is formed (see Fig. 5(a)). The exterior flow is steady and resembles that past a small bump (with the height of $0.2L$). Due to the streamlined shape of the bump, only minor separation in the exterior flow is observed near the trailing end (the tip of the filament). Inside the enclosed region, a recirculating flow is observed. At the specific time corresponding to the snapshot shown in Fig. 5(a) (i.e., the dimensionless time of 80), the velocity magnitude becomes rather small but the recirculating flow is still decaying slowly. The reason that it takes a long time for the recirculating flow to die out can be explained as follows. The decaying of the recirculating flow is dominated by diffusion and the characteristic decaying time scales as $L^2\nu^{-1}$. The dimensionless decaying time thus scales as $(L^2\nu^{-1})/(LU_\infty^{-1}) = Re = 400$. At $\gamma = 0.01$ (regular VIV mode), vortices shed periodically from the free end of the filament (see Fig. 5(b)). The dimensionless shedding frequency is about 0.2, which is comparable with that in flows over bluff bodies. This frequency is also the same as the oscillation frequency of the filament (since the vortex shedding acts as the excitation source). Moreover, the interaction between the vortex shed from the free end and the bottom wall also induces a small secondary vortex. At $\gamma = 0.1$ (static reconfiguration mode), a long shear layer remains attached to the free end of the highly deformed filament and the flow unsteadiness

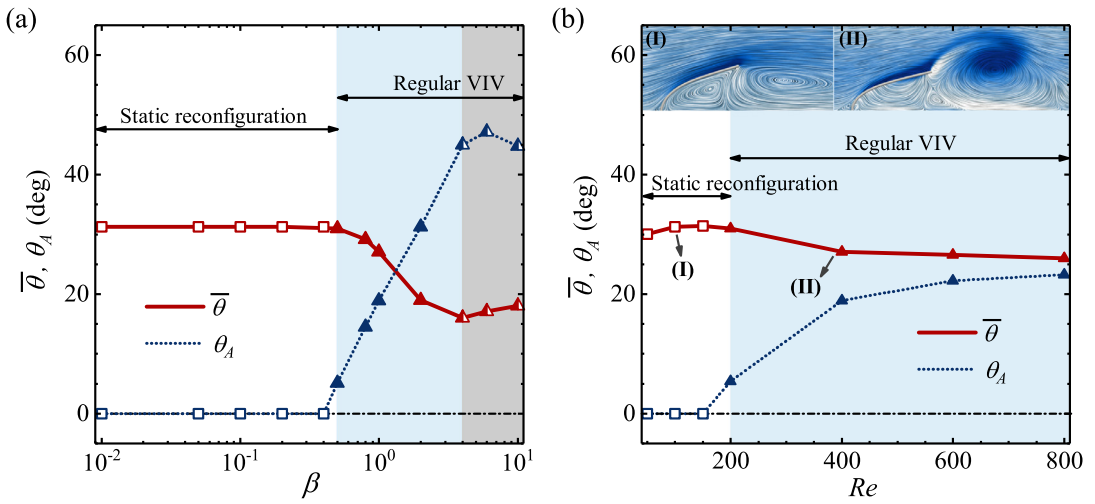

Fig. 6. Mean inclination angle $\bar{\theta}$ and amplitude of angular oscillation θ_A as a function of (a) β and (b) Re. The fixed control parameters are: (a) $\gamma = 0.01$ and $Re = 400$, and (b) $\gamma = 0.01$ and $\beta = 1.0$. The symbols here are the same as those used in Fig. 3. The two insets in (b) show the wake structures for the cases of $Re = 100$ and $Re = 400$, respectively.

is not observed (see Fig. 5(c)). At $\gamma = 0.5$ (static reconfiguration mode), the filament behaves practically like a rigid one since the deformation is rather small (see Fig. 5(d)). However, due to the presence of the bottom wall, the flow is rather different from that past a bluff body in open space. The vortex shedding is not initiated at the free end. Instead, it is triggered by the shear layer instability at a position that is further downstream. By probing the flow field at a position about half body length downstream of the tip, it is found that the vortex shedding frequency is roughly 80% of that in the regular VIV mode. The vorticity fluctuation magnitude, however, is only about one third of that in the regular VIV mode. Please note that the oscillation of the filament is undetected in this case. This is because the excitation source is too remote from the filament and is also too weak.

The effect of mass ratio on the dynamic behaviors is shown in Fig. 6(a), for $\gamma = 0.01$ and $Re = 400$. As can be seen from this figure, the static reconfiguration mode is observed at $\beta < 0.5$. Within this range of β, the mean inclination angle is insensitive to the variation of β and reaches a constant of 32°. With the increase of mass ratio beyond the value of 0.5, the dynamic behavior transits from the static reconfiguration mode to the regular VIV mode. The periodic and quasi-periodic oscillations are observed in the mass ratio ranges of $0.5 \leq \beta < 4.0$ and $\beta \geq 4.0$, respectively. For the periodic oscillation, θ_A increases monotonically with increasing β, while the opposite trend is found in $\bar{\theta}$. For the quasi-periodic oscillation, $\bar{\theta}$ and θ_A only vary slightly with increasing β.

The effect of Re on the dynamic behaviors is shown in Fig. 6(b), for $\gamma = 0.01$ and $\beta = 1.0$. From this figure, it is seen that for $Re < 200$, the static reconfiguration mode is observed and the flow around the filament is steady. When $Re \geq 200$, the filament transits to the regular VIV mode and the flow becomes unsteady with periodic vortex shedding at the free end. This critical Reynolds number for initiating vortex shedding is much higher than that of the flows past bluff bodies in open space (e.g. for flow past a circular cylinder this number is around 47). We believe that the presence of a solid wall is the primary reason for the higher critical Reynolds number. In the case of the cylinder in open space, the interaction between two shear layers eventually leads to instability and unsteadiness. In the case of the wall-mounted filament, the interaction between one shear layer and the ground somehow inhibits the aforementioned instability. Besides, the reconfiguration of the filament also plays a minor role in raising the critical Reynolds number, since a more streamlined shape may suppress flow separation to some extent.

It should be noted that the "effect of Reynolds number" studied here is actually the combined effects of Re and boundary layer thickness. The variation of Re unavoidably results in the change of boundary thickness (since the filament is always placed at a fixed distance from the entrance). We conjecture that the dynamic behavior of the filament largely depends on the value of Re, while the boundary layer thickness only plays a secondary role here. A more rigorous study on the isolated effect of Re can be done by changing the position of the filament to offset the change of boundary layer thickness. Such investigation has not been conducted in the present work.

We also perform parameter sweeps in the two-dimensional parameter space spanned by the bending rigidity and the mass ratio at $Re = 400$. Different modes of dynamic behavior in the space of (γ, β) are displayed in Fig. 7. At low density ratios ($\beta < 0.2$), the lodging mode and the static reconfiguration mode occupy the left half and right half, respectively. The threshold value of γ for the mode transition is around 1.5×10^{-3}. At high mass ratios ($\beta > 0.2$), the lodging mode, the regular VIV mode and the static reconfiguration mode occupy the left, intermediate and right columns, respectively. The threshold value of γ for the transition from the lodging mode to the regular VIV mode depends on the value of β. The regions for the regular VIV and the static reconfiguration modes are separated (approximately) by a straight demarcation

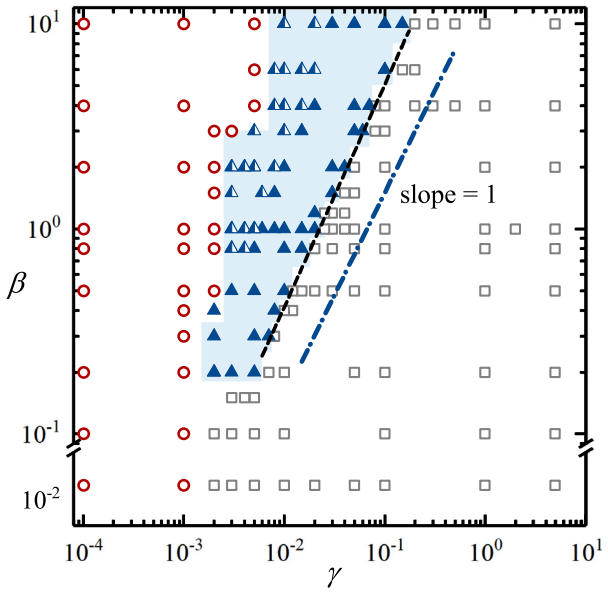

Fig. 7. A map for the modes of dynamic behavior in the two-dimensional space of (γ, β) at $Re = 400$. Circles, semi-hollow triangles, solid triangles and squares denote the lodging mode, the regular VIV mode (quasi-periodic oscillation), the regular VIV mode (periodic oscillation), and the static reconfiguration mode, respectively.

line with the slope of 1. The explanations on the demarcation lines that separate the two modes of dynamic behavior are provided here in the context of the competitions among moments of elastic, pressure and inertial forces. The moments (per unit span) of elastic, pressure and inertial forces scale as $M_e \sim B/L$, $M_p \sim \rho_f U_\infty^2 L^2$ and $M_i \sim \rho_s U_\infty^2 \delta L = \beta M_p$, respectively. When β is relatively low, the transition from the lodging mode to the static reconfiguration mode occurs at a threshold ratio of elastic moment to pressure moment (i.e., $M_e/M_p = B/\rho_f U_\infty^2 L^3 = \gamma$). When β is relatively high, the transition from the regular VIV mode to the static reconfiguration mode occurs at a threshold ratio of elastic moment to inertia moment (i.e., $M_e/M_i = \gamma/\beta$). The demarcation line that separates the lodging mode and the regular VIV mode at relatively high mass ratios looks like a staircase. A physical interpretation on such separation boundary is still lacking.

4.1.2. Frequency lock-in phenomenon

In the studies of fluid-induced oscillation, the phenomenon that the vortex shedding frequency synchronizes with the natural frequency of the structure is termed lock-in Kaneko et al. (2014). Here we explore whether the lock-in phenomenon occurs in the single-filament system.

The natural frequencies of the present system are first estimated by those for a cantilever Euler–Bernoulli beam in vacuum. The ith-order dimensionless natural frequency is given by:

$$f_{ni} = \frac{\tilde{f}_{ni} L}{U_\infty} = \frac{k_i^2}{2\pi}\sqrt{\frac{\gamma}{\beta}}, \text{ with } \cos k_i \cosh k_i + 1 = 0. \tag{9}$$

Here $\tilde{f}_{ni}$ is the dimensional natural frequency. The coefficients for the first and second natural frequencies are $k_1 = 1.875$ and $k_2 = 4.694$, respectively. For a cantilever beam immersed in the fluid, the natural frequencies are modulated by the effect of added mass. The modulated ith-order dimensionless natural frequency can be written as:

$$f_{ni}^* = \frac{k_i^2}{2\pi}\sqrt{\frac{\gamma}{\beta + C_m \cdot \pi/4}}, \tag{10}$$

where $C_m = 1$ (Luhar and Nepf, 2016).

Besides the added mass effect, three other effects can also lead to the deviation of the natural frequencies from f_{ni}. They are the non-linear effect due to large-amplitude oscillation, the flow-induced damping effect due to drag, and the added stiffness effect due to mean deflection (prestress). The influence of non-linear effect on the value of natural frequency is very hard to analyze theoretically. The flow-induced damping effect tends to reduce the natural frequency, while the added stiffness effect tends to increase the natural frequency (Heylen et al., 1998). Thus, the latter two effects may cancel each other out to some extent. The flow-induced damping and added stiffness effects can be evaluated experimentally (Jin et al., 2018c; Saiidi et al., 1994). However, the empirical expressions to account for these two effects are usually not valid universally.

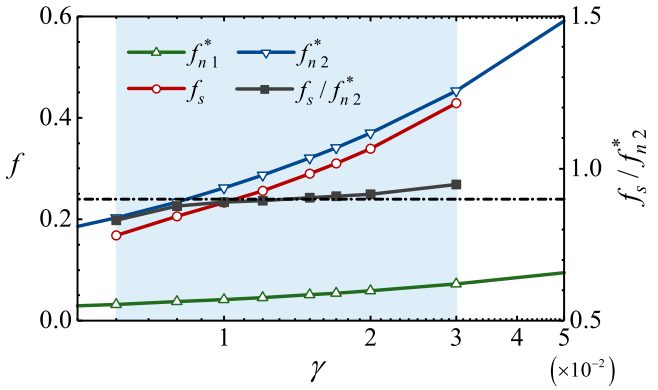

Fig. 8. Frequency lock-in phenomenon in the regular VIV mode. The shaded region denotes the range of rigidity where periodic oscillation occurs. The dash-dotted horizontal line represents the mean value of f_s/f_{n2}^*.

Here we take f_{ni}^* as the (approximate) natural frequencies and examine the closeness of the oscillation frequency with the (first and second) natural frequencies. A series of periodic oscillation cases in the regular VIV mode are considered here, with the bending rigidity ranging from 0.006 to 0.03. As shown in Fig. 8, the oscillation frequency f_s is always between 0.15 to 0.4. This observed range of dimensionless frequencies is in agreement with the typical Strouhal number for vortex shedding over a bluff body (which is around 0.2). From this figure, it is also seen that the oscillation frequency is close to the second natural frequency f_{n2}^* and the frequency ratio f_s/f_{n2}^* is nearly a constant around 0.91.

Since the oscillation frequency is sufficiently close to f_{n2}^* within the entire range of bending rigidity, we are inclined to believe that in the regular VIV mode it is locked onto the second natural frequency of the structure. This can be further supported by the fact that the waveform of second bending mode is clearly exhibited in the oscillation (cf. Fig. 3(b)). Such oscillation is superimposed on a highly deformed configuration in which the posterior part is almost in parallel with the direction of the incoming flow. The shape of the oscillating filament found here is in agreement with that found in the previous study on a flag placed in a transverse flow (Leclercq et al., 2018). However, owing to the inaccuracy in the evaluation of natural frequency, whether the lock-in phenomenon indeed occurs is still contestable.

The lock-in phenomenon near the first natural frequency has not been observed in this study. This can be explained by the fact that the vortex shedding becomes rather weak when the filament is less deformed with a nearly upright orientation (cf. Fig. 5(d)). At much higher Reynolds numbers, however, the vortex shedding in such configuration can be much stronger and the lock-in phenomenon near the first natural frequency may occur (Py et al., 2006; Jin et al., 2018c).

4.2. Dual-filament system

4.2.1. Influence of bending rigidity in the dual-filament system

The variations of the mean inclination angle and amplitude of angular oscillation with rigidity for the dual-filament system are shown in Fig. 9. From this figure, four modes of the dynamic behaviors, namely, lodging, regular VIV, static reconfiguration and cavity oscillation, can be identified. The amplitude envelopes corresponding to the four different modes are displayed in Fig. 10. At low bending rigidity, both filaments fall flat on the ground and the lodging mode is observed (see Fig. 10(a)). At intermediate bending rigidity, the regular VIV mode emerges with large static deformation and large oscillation amplitude (see Fig. 10(b)). The static deformations and oscillation amplitudes in both filaments are comparable, while the oscillation frequencies are identical. Similar to that observed in the single-filament system, the oscillations can be further categorized into the periodic and the quasi-periodic sub-types. With the increase of bending rigidity, the oscillations disappear and the static reconfiguration mode is observed. It is also observed that within certain range of bending rigidity, the downstream filament bends towards the upstream direction (see Fig. 9(a) and Fig. 10(c)). This interesting phenomenon will be further addressed later. When the bending rigidity increases further, a distinct mode of the dual-filament system emerges. It is termed the "cavity oscillation" mode in this paper. An explanation on this name will be provided later. It is worth noting that this mode does not exist in the single-filament system. In this oscillation mode, the static deformations of both filaments are rather small. The oscillation amplitude of the upstream filament is also small (less than 3°). In contrast, the oscillation amplitude of the downstream filament is quite large (the amplitude in this mode can reach up to 20°, which is comparable to that in the regular VIV mode) (see Fig. 9(d)). At even higher bending rigidity, the oscillations disappear again and the static reconfiguration mode reemerges (with very small static deformations in both filaments).

The wake structures corresponding to different bending rigidities are shown in Fig. 11. The wake structures for the lodging, regular VIV, and static reconfiguration modes are similar to those in the single-filament system (cf. Fig. 5). For the regular VIV mode, it is seen that there exists a phase difference between the oscillations of the upstream and

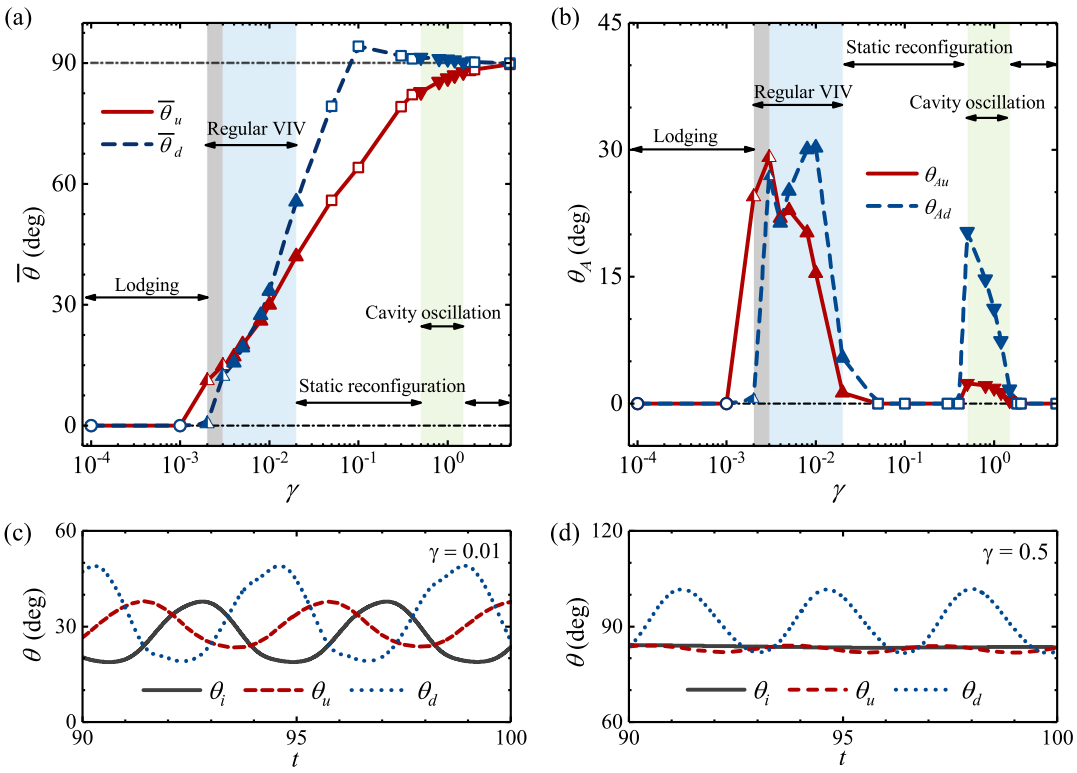

Fig. 9. Dynamic behaviors of the dual-filament system at different bending rigidities. (a) Mean inclination angles of the upstream and downstream filament as a function of γ. (b) Amplitudes of angular oscillation of the upstream and downstream filament as a function of γ. (c) Time histories of the inclination angles in the regular VIV mode. (d) Time histories of the inclination angles in the cavity oscillation mode. Circles, upward-facing triangles, squares and downward-facing triangles represent the lodging, regular VIV, static reconfiguration and cavity oscillation modes, respectively. Within the regular VIV regime, the semi-hollow and solid symbols represent the quasi-periodic and periodic oscillations, respectively. The subscripts "*i*", "*u*" and "*d*" in the variables denote the quantity of the filament in the single-filament system and the quantities of the upstream and downstream filaments, respectively. The fixed control parameters are: $\beta = 1.0$, $Re = 400$, $d = 1.0$.

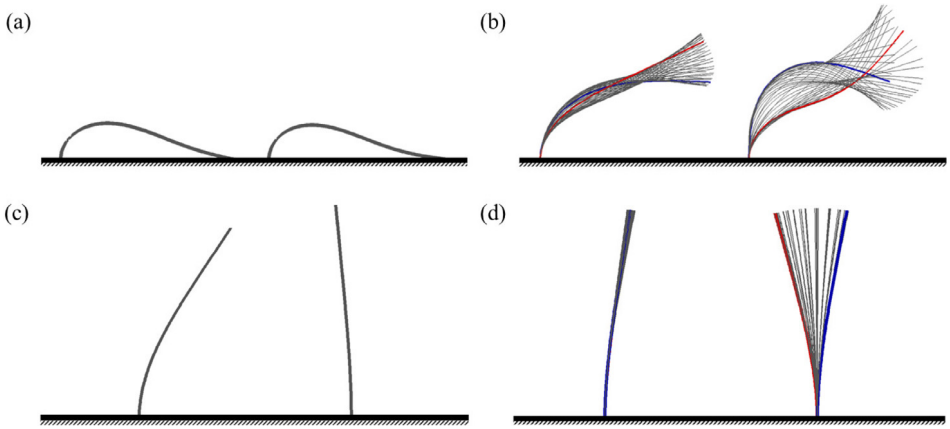

Fig. 10. Amplitude envelops at different rigidities corresponding to the (a) lodging ($\gamma = 0.001$), (b) regular VIV ($\gamma = 0.01$), (c) static reconfiguration ($\gamma = 0.1$) and (d) cavity oscillation ($\gamma = 1.0$) modes. The fixed control parameters are: $\beta = 1.0$, $Re = 400$, $d = 1.0$.

downstream filaments (see Fig. 11(b) and also Fig. 9(c)). For the static reconfiguration mode, the wake structure hints that the "abnormal" bending of the downstream filament is associated with the recirculating (inverse) flow induced by the upstream filament (see Fig. 11(c)). As to the cavity oscillation mode, it is seen that the wake structure is very different from that of the regular VIV mode (see Fig. 11(d)). In this mode, the vortex shedding pattern bears a remarkably

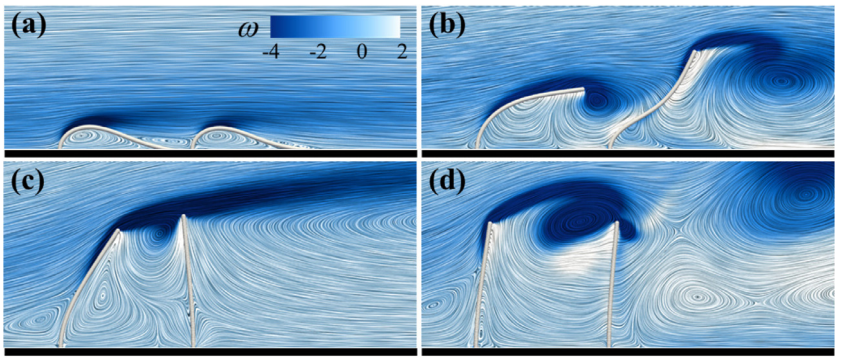

Fig. 11. Representative wake structures of the two-filament system at different rigidities corresponding to the four different modes: (a) $\gamma = 0.001$ (lodging); (b) $\gamma = 0.01$ (regular VIV); (c) $\gamma = 0.1$ (static reconfiguration); (d) $\gamma = 0.5$ (cavity oscillation). The fixed control parameters are: $\beta = 1.0$, $Re = 400$, $d = 1.0$. The contours of dimensionless vorticity and the streamlines are used to visualize the wake structures.

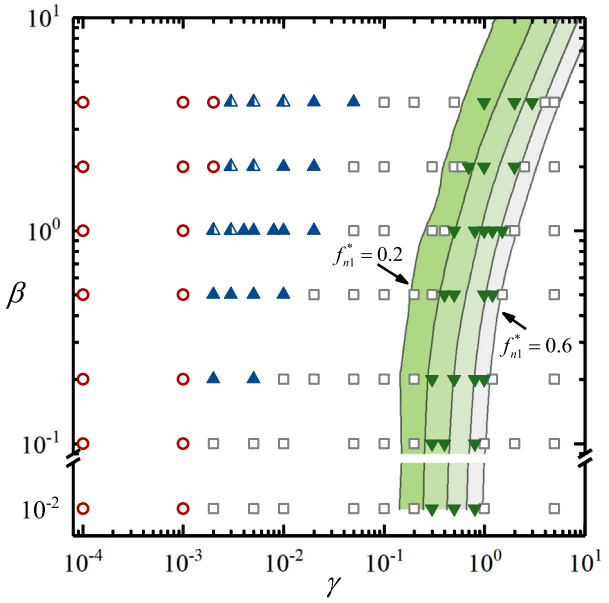

Fig. 12. A map for the modes of dynamic behavior in the two-dimensional parameter space of (γ, β) for the dual-filament system. Circles, semi-hollow triangles, solid upward triangles, squares and solid downward triangles denote the lodging mode, the regular VIV mode (quasi-periodic oscillation), the regular VIV mode (periodic oscillation), the static reconfiguration mode, and the cavity oscillation mode, respectively. The contours which represent the first natural frequency in the range of 0.2 and 0.6 are plotted for illustration purpose. The fixed control parameters are: $Re = 400$ and $d = 1.0$.

close resemblance to that of the open-cavity flow, and is very dissimilar to that of flow over a bluff body (as that seen in the regular VIV mode. This is the reason for naming it the "cavity oscillation" mode. Since the vortex shedding also acts as the excitation source in this oscillation mode, it can be regarded as another case of VIV. Actually, the geometric configuration of the dual-filament system is somewhat different from a standard open cavity. Instead, it can be regarded as the combination of a forward-facing step, an open cavity and a backward-facing step.

A map for the modes of dynamic behavior of the dual-filament system in the two-dimensional parameter space of (γ, β) is shown in Fig. 12. In comparison with the map for the single-filament system, the regions occupied by the lodging and regular VIV modes are almost unaffected by the addition of the second filament. The cavity oscillation mode occupies a narrow banded region which is embedded into the region of the static reconfiguration mode. Further investigation indicates that this banded region corresponds to a narrow range of first natural frequency in between 0.2 and 0.6. This hints the occurrence of frequency lock-in phenomenon. The frequency lock-in phenomenon in the dual-filament system will be further addressed in Section 4.2.3.

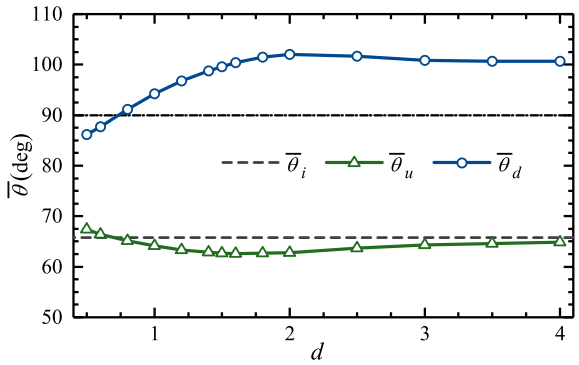

Fig. 13. Effect of interspace on the mean inclination angles of the two filaments in the static reconfiguration mode. The subscripts "*i*", "*u*" and "*d*" in the variables denote the quantity of the filament in the single-filament system and the quantities of the upstream and downstream filaments, respectively. The fixed control parameters are: $\beta = 1.0$, $\gamma = 0.1$, $Re = 400$.

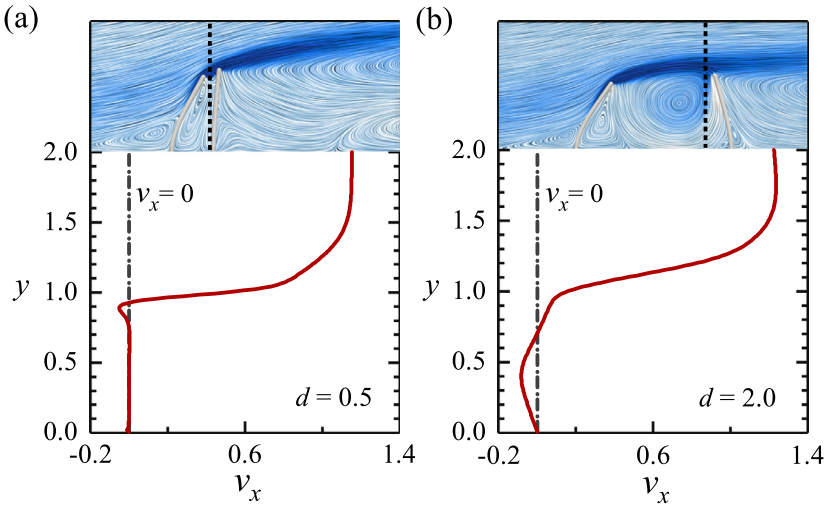

Fig. 14. Profiles of streamwise velocity along a vertical line that is slightly upstream of the downstream filament: (a) $d = 0.5$; (b) $d = 2.0$. For both cases, the distances from the vertical line to the tip of the downstream filament is $0.1L$. The fixed control parameters are: $\beta = 1.0$, $\gamma = 0.1$, $Re = 400$. The two insets in (a) and (b) show the wake structures for the cases of $d = 0.5$ and $d = 2.0$, respectively. The positions of the vertical lines are also shown in the two insets.

4.2.2. Influences of interspace in the dual-filament system

In the coupled systems with two filaments, the interspace d also plays a critical role in determining the dynamic behaviors. The static reconfiguration mode, the regular VIV mode, and the cavity oscillation mode will be addressed separately.

For the static reconfiguration mode, the variations of mean inclination angles ($\bar{\theta}$) with d (for both filaments) are shown in Fig. 13. It is seen that within the entire range of interspace considered here ($0.5 \leq d \leq 4.0$), the static deformation of the upstream filament is very close to that of the filament in the single-filament system. Thus, the downstream filament only has minor effect on the reconfiguration of the upstream one. The static deformation of the downstream filament is much smaller, in comparison with that of the filament in the single-filament system. This can be explained intuitively by the shielding effect from the upstream filament.

In the range of $0.8 \leq d \leq 4.0$, the "abnormal" bending (i.e., bending towards the upstream direction) is observed in the downstream filament. This can be explained by the recirculating (inverse) flow induced by the upstream filament. To provide some quantitative support, the streamwise velocity profiles along one vertical line slightly upstream of the downstream filament are plotted, for the cases of $d = 0.5$ and $d = 2.0$ (see Fig. 14). It turns out that the inverse flow in front of the downstream filament is only evident in the case of $d = 2.0$ (the case with "abnormal" bending).

For the regular VIV mode, the variations of $\bar{\theta}$ and θ_A with d (for both filaments) are shown in Fig. 15(a). It is observed that the mean inclination angles of both filaments undulate slightly with increasing d when the interspace is narrow and level off when $d > 2.5$. The static deformation of the downstream filament is always smaller than that of the upstream one due to the shielding effect. The oscillation amplitudes of both filaments also first undulate slightly with increasing d

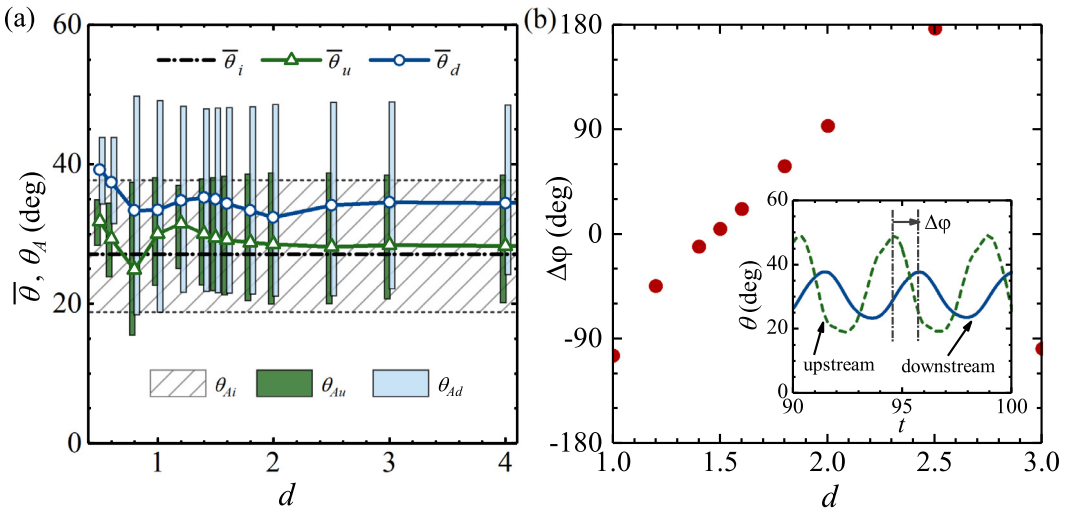

Fig. 15. Effect of interspace on the coupled behavior in the regular VIV mode (periodic oscillation). (a) Mean inclination angles and amplitudes of angular oscillation as a function of d. The subscripts "i", "u" and "d" in the variables denote the filament in the single-filament system, the upstream and downstream filaments in the dual-filament system, respectively. (b) The phase difference between the oscillations of the two filaments as a function of d. In (a), the mean inclination angles and amplitudes of angular oscillations are represented by curves and histograms, respectively. The inset in (b) shows the definition of the phase difference between the two filaments. The fixed control parameters are: $\beta = 1.0$, $\gamma = 0.01$, $Re = 400$.

and then level off. The oscillation amplitude of the downstream filament is always larger than that of the upstream one. The amplification of the oscillation amplitude in the downstream filament is due to the periodic excitation generated by the vortex shedding over the upstream one. The phase difference $\Delta\varphi$ between the oscillations of the two filaments as a function of d is shown in Fig. 15(b). It is seen that a linear dependence exists between the phase difference and the interspace. Thus, for the regular VIV mode, the variation of interspace only modulates the phase difference between the oscillations of the two filaments, whereas the dynamic behavior of the system is not qualitatively changed.

Here we provide a physical explanation on the linear dependency between the phase difference and the interspace. For an advection-dominated flow, it is reasonable to assume that the phase difference $\Delta\varphi$ between the oscillations of the two filaments is caused by the time delay δt that scales as D/U_{conv}, where the convection velocity U_{conv} is proportional to U_∞. Thus, $\Delta\varphi \approx 2\pi f \delta t \approx a_0 2\pi f D/U_\infty = (a_0 2\pi St) \cdot d$, where both a_0 and Strouhal number ($St = fL/U_\infty$) can be regarded as constants.

For the cavity oscillation mode, the influence of interspace on the dynamic behavior becomes more complicated. The variations of the mean inclination angles and amplitudes of angular oscillation with d are shown in Fig. 16(a). It is seen the static deformation of the upstream filament is almost the same as that in the single-filament system, while the static deformation of the downstream one is negligible. Thus, both filaments practically oscillate in the horizontal direction (if such oscillations can be initiated). Actually, the oscillations can only be initiated if d lies in the ranges of $1.0 \leq d \leq 2.2$ and $3.5 \leq d \leq 4.0$, respectively. The oscillation amplitude of the downstream filament is always much larger than that of the upstream one. When d lies out of the two ranges above, the amplitudes of oscillation are reduced to zero and the static reconfiguration mode is observed. Thus, d is a key parameter which governs the mode switching between cavity oscillation and static reconfiguration.

To further elucidate the role that the interspace plays in mode switching, we also perform parameter sweeps on the two dimensional space of (γ, d). The map for the modes of dynamic behavior in the space of (γ, d) is displayed in Fig. 16(b). It is seen that the cavity oscillation mode occupies two banded regions (branches) that are interspersed in the region occupied by the static reconfiguration mode. The lower branch covers the entire parameter range, while the upper branch only exists at relative wide interspaces ($d > 2.5$). A physical explanation of this finding will be provided in Section 4.2.3.

4.2.3. Frequency lock-in phenomenon in the dual-filament system

In Section 4.1.2, it is found that in the single-filament system, the oscillating frequency in the regular VIV mode is always locked onto the second natural frequency. In this section, we explore whether the frequency lock-in phenomenon also occurs in the dual-filament system. The regular VIV mode and the cavity oscillation mode will be addressed separately.

For the regular VIV mode (periodic oscillation), we consider two series of cases: (a) $d = 1.0$, with the bending rigidity ranging from 0.003 to 0.02, and (b) $\gamma = 0.01$, with the interspace ranging from 0.5 to 5.0. All other control parameters such as β and Re are fixed. We examine the closeness of the oscillation frequencies to the (first or second) natural frequency. As shown in Fig. 17(a) and Fig. 17(b), the oscillation frequencies are always locked onto the second natural frequency (in the entire ranges of rigidity and interspace studied here). This finding is in consistent with the frequency lock-in

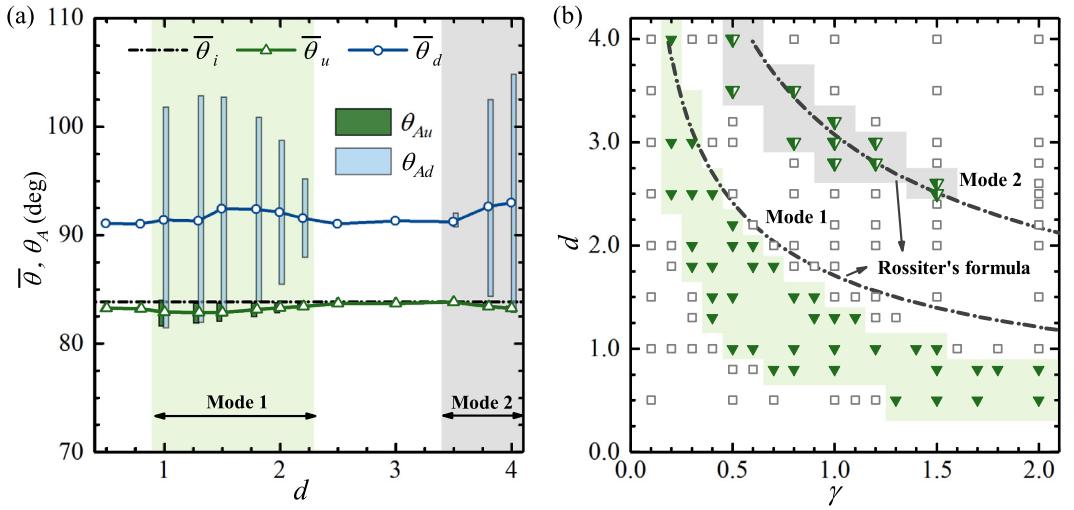

Fig. 16. Effect of interspace on the coupled behavior in the cavity oscillation mode. (a) Mean inclination angle and amplitude of angular oscillation as a function of d. The subscripts "i", "u" and "d" in the variables denote the filament in the single-filament system, the upstream and downstream filaments in the dual-filament system, respectively. The mean inclination angles and amplitudes of angular oscillation are represented by curves and histograms, respectively. The fixed parameters are: $\beta = 1.0$, $\gamma = 0.5$, $Re = 400$. (b) The map for the modes of dynamic behavior in the space of (γ, d). Squares, solid triangles and semi-hollow triangles represent the static reconfiguration mode, the first and second Rossiter modes of the cavity oscillation mode, respectively. The dash-dotted lines represent the frequency lock-in condition determined by using Rossiter's formula. The fixed control parameters are: $\beta = 1.0$, $Re = 400$.

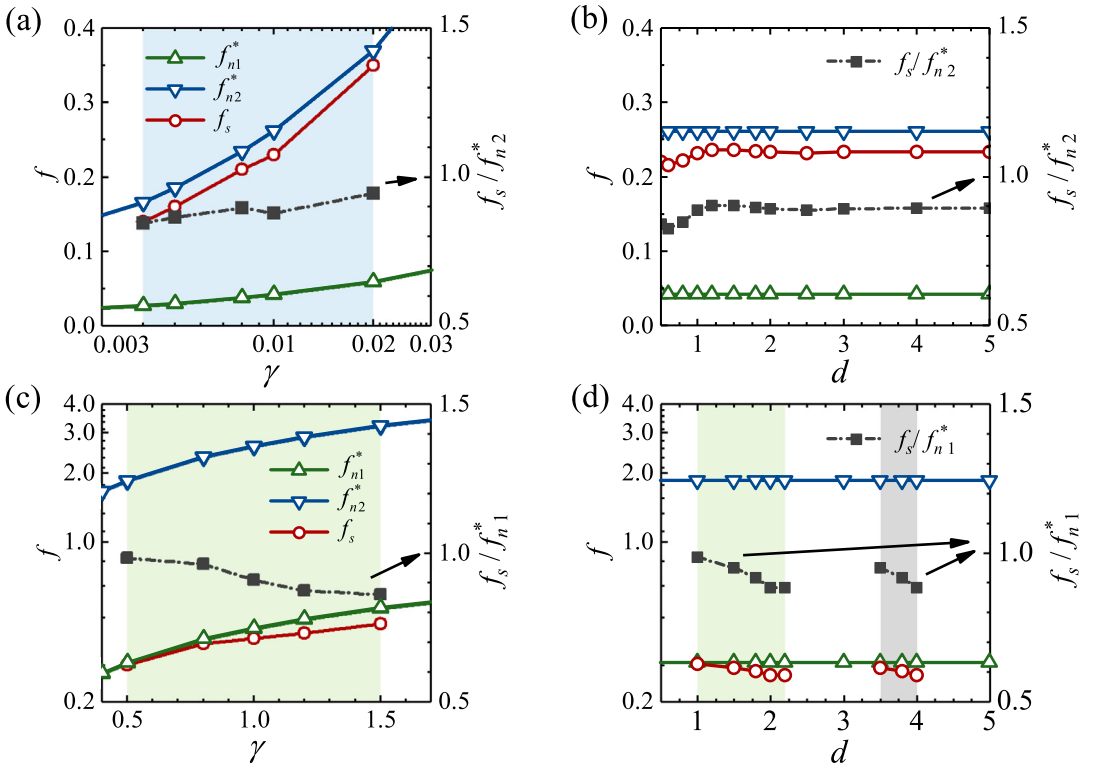

Fig. 17. Frequency lock-in phenomenon in the dual-filament system: regular VIV mode (periodic oscillation) ((a)–(b)); cavity oscillation mode ((c)–(d)). The oscillation frequency, the first and the second natural frequencies, and also the ratio of the oscillation frequency to the (second or first) natural frequency are plotted as a function of the dimensionless rigidity (in (a) and (c)), or as a function of the interspace (in (b) and (d)). The fixed parameters used are: $\beta = 1.0$, $Re = 400$.

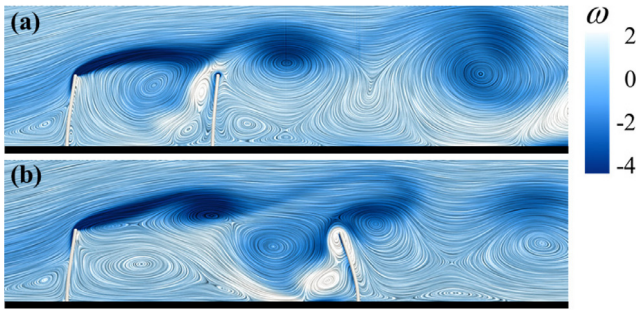

Fig. 18. Wake structures of the dual-filament system in the cavity oscillation mode at different interspaces: (a) $d = 2.0$ (first Rossiter mode), (b) $d = 4.0$ (second Rossiter mode). The fixed control parameters are: $\beta = 1.0$, $\gamma = 0.5$, $Re = 400$. The contours of dimensionless vorticity and the streamlines are used to visualize the wake structures.

phenomenon observed in the single-filament system (cf. Fig. 8). Therefore, for the regular VIV mode (periodic oscillation), the flow-induced interaction between the two filaments does not qualitatively change the frequency lock-in phenomenon.

For the cavity oscillation mode, we consider two series of cases: (a) $d = 1.0$, with the rigidity ranging from 0.5 to 1.5, and (b) $\gamma = 0.5$, with the interspace ranging from 0.5 to 5.0. We also examine the closeness of the oscillation frequencies to the (first or second) natural frequency. Please note that for the cases in the cavity oscillation mode, the theoretical expression of Eq. (10) may give a better prediction for the natural frequency (in comparison with the cases in the regular VIV mode). This is because that in the cavity oscillation mode the oscillation amplitude is smaller and the mean deflection is close to zero. As shown in Fig. 17(c) and Fig. 17(d), the oscillation frequencies are always locked onto the first natural frequency. This phenomenon is very similar to the "fluid-elastic" cavity oscillation reported in some previous studies, in which one or more walls of a open cavity underwent large elastic deformation (Rockwell and Naudascher, 1978).

The frequency selection mechanism in the cavity oscillation mode is further explained as follows. The dimensionless frequency of the open-cavity flow can be estimated by using the following semi-empirical formula (i.e., Rossiter's formula) (Gloerfelt, 2009):

$$f_c = \frac{\tilde{f}_c L}{U_\infty} = \frac{n-\alpha}{1/\kappa + M}\frac{U_\infty}{D}\cdot\frac{L}{U_\infty} = \frac{n-\alpha}{1/\kappa + M}\cdot\frac{1}{d}. \tag{11}$$

Here $\tilde{f}_c$ is the dimensional oscillating frequency of the open-cavity flow. M is the Mach number (which is zero for incompressible flows). n is an integer which represents the order of Rossiter mode (i.e., $n = 1, 2, \ldots$). κ and α are two empirical constants. By calibration using the experimental data, the values of $\kappa = 0.57$ and $\alpha = 0.25$ are found to yield satisfactory results (Gloerfelt, 2009).

The curves for the frequency lock-in condition in the space of (γ, d) can be obtained by setting $f_c = f^*_{n1}$. Two such curves, which represent the lock-in condition for the first and second Rossiter modes (i.e., $n = 1$ and $n = 2$), are plotted in Fig. 16(b). From this figure, it is seen that the two banded regions of the cavity oscillation mode are reasonably close to the two curves signifying the frequency lock-in condition. The two possible reasons for the deviation are: (a) the difference between the configurations of the dual-filament system and that of the standard open cavity, and (b) the uncertainty in the values of the empirical constants. We believe that the deviation can be reduced if some modifications are made to the Rossiter's formula by taking these two factors into consideration. Some typical features of the open-cavity flow are also exhibited in Fig. 16(b). For example, the coexistence of several Rossiter modes in a certain range of d and the existence of a threshold value of d above which higher Rossiter mode emerges.

The wake structures associated with the first and second Rossiter modes are compared in Fig. 18. It is seen that the number of large vortex structures trapped in the "cavity" formed by the two filaments is in consistent with the Rossiter mode number.

5. Conclusions

We numerically studied the dynamics of both single and dual wall-mounted flexible filaments in a laminar boundary layer. The dependence of dynamic behaviors on some control parameters (such as bending rigidity, mass ratio, Reynolds number and interspace between the two filaments) were explored. For the single-filament system, three modes of dynamic behavior, namely, lodging, regular VIV and static reconfiguration, have been identified. For the dual-filament system, in addition to the three modes above, another distinct mode - cavity oscillation mode, was also identified.

The frequency lock-in phenomenon was observed in both the regular VIV mode and the cavity oscillation mode. For the regular VIV mode, the oscillating frequency was always locked onto the second natural frequency. For the cavity oscillation mode, the oscillating frequency was always locked onto the first natural frequency. For both oscillation modes, the vortex shedding was found to be the excitation source. For the regular VIV mode, the wake pattern resembled that

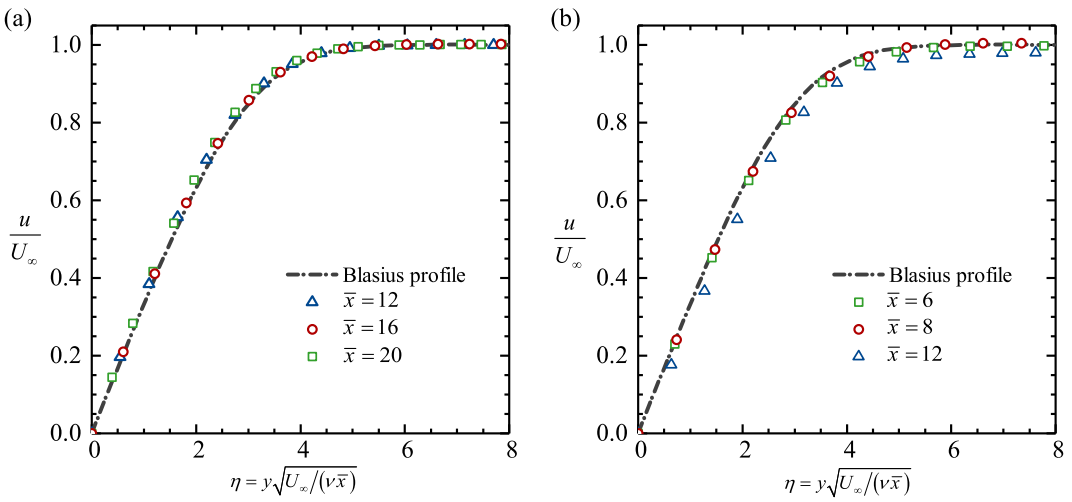

Fig. A.1. Dimensionless velocity profiles of (a) the undisturbed boundary layer and (b) the disturbed boundary layer (with a single wall-mounted flexible filament at $\bar{x} = 15$), at different streamwise positions obtained from the numerical simulation. Here $\bar{x}$ denotes the dimensionless distance from the entrance. The solid lines denote the Blasius solution. For the case without the filament, the Reynolds number based on a distance of $15L$ is 6000. For the case with a single filament, the Reynolds number based on L is 400. The mass ratio (β) and dimensionless bending rigidity (γ) of the filament are 1.0 and 0.01, respectively.

of the vortex shedding over a bluff-body. In contrast, for the cavity oscillation mode, the wake pattern resembled that of the vortex shedding over an open cavity.

There are several interesting avenues for further research. First, the coherent waving interactions between the boundary layer flow and a much larger array of flexible structures should be investigated. Second, the restriction to two dimensions should be released by conducting three-dimensional simulations. Third, a more accurate model for predicting the occurrence of cavity oscillation is needed.

Declaration of competing interest

The authors declare that they have no known competing financial interests or personal relationships that could have appeared to influence the work reported in this paper.

Acknowledgments

This work was supported by National Natural Science Foundation of China under Projects Nos. 11772338, 10732090, 11023001, 11232011, and 11372331, Chinese Academy of Sciences under Projects Nos. KJCX-SW-L08, KJCX3-SYW-S01 and XDB22040104. We would like to thank the National Supercomputing Center in Tianjin (NSCC-TJ) for the allocation of computing time.

Appendix. Validation cases and grid, time step, and domain independence tests

To ensure that the mesh resolution in the present study is sufficient to resolve the boundary layer, the velocity profiles for the undisturbed and disturbed boundary layer flows are compared with the Blasius solution. For the case without the filament, the Reynolds number based on a distance of $x = 15L$ is 6000. For the case with a single wall-mounted filament, the Reynolds number based on L is 400. Fig. A.1(a) shows the dimensionless velocity profiles at different distances from the entrance, for the case without the filament. A perfect match between the numerical and the Blasius solutions is seen at all positions. For the case with one filament mounted on the bottom wall, the velocity profiles at various upstream positions are also compared with the Blasius solution in Fig. A.1(b). Some deviations from the Blasius solution are found at the positions very close to the filament. At the positions far enough away from the filament, the velocity profiles matches the Blasius solution well. Moreover, we also conduct a domain-sensitivity test on the boundary layer flow (without the filament) at the lowest Reynolds number considered in this work. The Reynolds number based on $x = 15L$ is 750. It turns out that the domain size used in the simulation is large enough for achieving a domain-independent solution, even for the case with the thickest boundary layer. For brevity, the result of this test is not presented in the appendix.

To ensure that the results of FSI simulation are (almost) independent of the mesh resolution, a mesh convergence test is conducted on a representative case of the single-filament system. The control parameters are: $\beta = 1.0$, $\gamma = 0.01$ and $Re = 800$. The Reynolds number of 800 is the highest one that is considered in this study. Besides the original mesh that

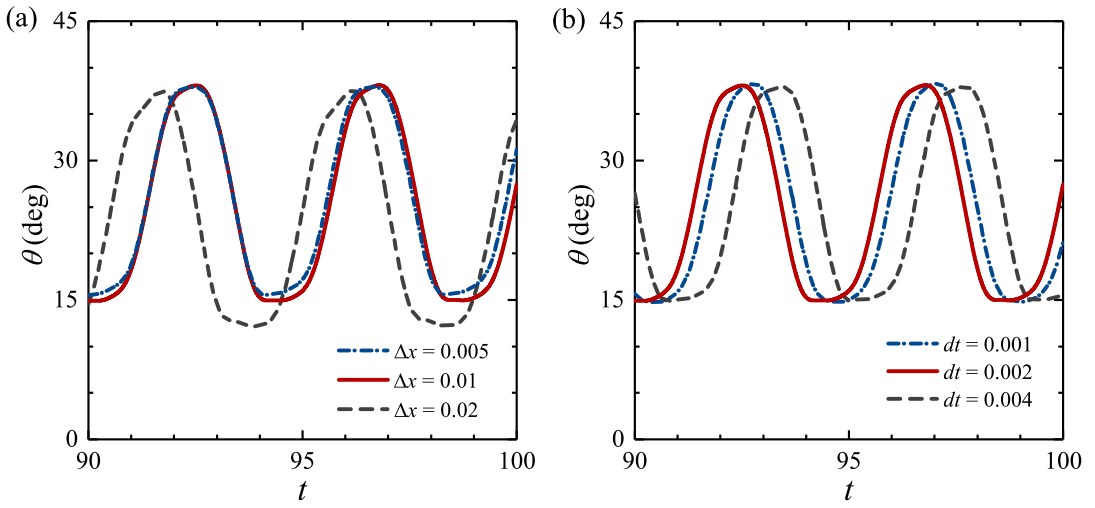

Fig. A.2. Results of the mesh and time step size independence tests. (a) Time histories of the inclination angle θ obtained by using three different meshes. The dashed, solid and dash-dotted lines represent the results for the grid width of 0.02L, 0.01L and 0.005L, respectively. (b) Time histories of the inclination angle θ obtained by using three different time step sizes. The dashed, solid and dash-dotted lines represent the results for the time step of 0.004, 0.002 and 0.001, respectively.

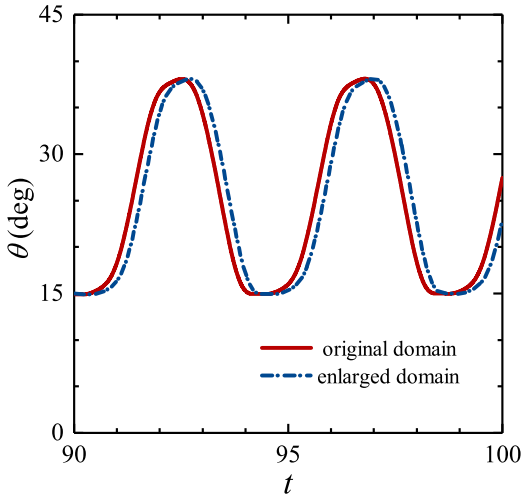

Fig. A.3. Results of the test on the sensitivity of solution to domain size. Time histories of the inclination angle θ obtained by using two different computational domains. The solid and the dash-dotted lines denote the results obtained by using the original domain and the enlarged domain, respectively.

is used in the simulation, one coarse mesh and one refined mesh are also generated. The grid widths in the vicinity of the filament are 0.02L, and 0.005L, for the coarse and refined meshes, respectively. (The resolutions in the regions far away from the filament are also adjusted proportionally according to the setting of the original mesh.) The dimensionless time step is fixed to 0.004 and 0.001 for the coarse and refined meshes, respectively. The time histories of the tip inclination angle (θ) obtained by using three different meshes are shown in Fig. A.2(a). The discrepancy between the results obtained with the intermediate (original) mesh and the coarse mesh is clearly visible. The discrepancy between the results obtained with the refined mesh and the intermediate (original) mesh becomes negligible. Thus, the intermediate mesh with the grid width of 0.01L is used in the simulation of the present study.

Similarly, a time step independence test is conducted on the same case. The mesh with the grid width of 0.01L is used. The time histories of the tip inclination angle (θ) obtained by using three different time step sizes ($\Delta t = 0.004$, $\Delta t = 0.002$ and $\Delta t = 0.001$) are shown in Fig. A.2(b). The time step convergence behavior is clearly visible from this figure. The solutions obtained with $\Delta t = 0.002$ and $\Delta t = 0.001$ are sufficiently close to each other in terms of oscillation amplitude and period. A small phase difference between the two is originated from the slightly different time at which the oscillation is triggered. Thus, the time step of $\Delta t = 0.002$ is used in the simulation of the present study.

In addition, the sensitivity of the FSI solution to the domain size is also tested on the same case. Both the original computational domain of $[0, 32L] \times [0, 8L]$ and an enlarged domain of $[0, 40L] \times [0, 10L]$ are used for the test. It should be noticed that for the two domains used, the distances from the entrance to the filament is fixed and thus the boundary layer thickness at the position of the filament is the same. Fig. A.3 displays the time histories of θ obtained by using two different computational domains. It is seen that the two results agree very well with each other. Again, a small phase difference between the two is originated from the slightly different time at which the oscillation is triggered. Thus, the original computational domain is sufficiently large for ensuring domain independence.

References

Alben, S., Shelley, M.J., 2008. Flapping states of a flag in an inviscid fluid: bistability and the transition to chaos. Phys. Rev. Lett. 100 (7), 074301.

Alben, S., Shelley, M.J., Zhang, J., 2002. Drag reduction through self-similar bending of a flexible body. Nature 420, 479–481.

Belmonte, A., Shelley, M.J., Eldakar, S.T., Wiggins, C.H., 2001. Dynamic patterns and self-knotting of a driven hanging chain. Phys. Rev. Lett. 87, 114301.

Connell, B.S.H., Yue, D.K.P., 2007. Flapping dynamics of a flag in a uniform stream. J. Fluid Mech. 581, 33–67.

Dai, L.Z., He, G.W., Zhang, X., 2016. Self-propelled swimming of a flexible plunging foil near a solid wall. Bioinsipration Biomim. 11, 046005.

Dai, L.Z., He, G.W., Zhang, X., Zhang, X., 2018a. Intermittent locomotion of a fish-like swimmer driven by passive elastic mechanism. Bioinsipration Biomim. 13, 056011.

Dai, L.Z., He, G.W., Zhang, X., Zhang, X., 2018b. Stable formations of self-propelled fish-like swimmers induced by hydrodynamic interactions. J. R. Soc. Interface 15, 20180490.

De Langre, E., 2008. Effects of wind on plants. Annu. Rev. Fluid Mech. 40, 141–168.

Favier, J., Li, C., Kamps, L., Revell, A., J., O., Brucker, C., 2017. The PELskin project - part I: fluid-structure interaction for a row of flexible flaps: a reference study in oscillating channel flow. Meccanica 52, 1767–1780.

Gloerfelt, X., 2009. Cavity noise. In: VKI Lecture Series, vol. 3.

Gosselin, F.P., 2019. Mechanics of a plant in fluid flow. J. Exp. Bot. 70, 3533–3548.

Gosselin, F.P., De Langre, E., Machado-Almeida, B.A., 2010. Drag reduction of flexible plates by reconfiguration. J. Fluid Mech. 650, 319–341.

Henriquez, S., Barrero-Gil, A., 2014. Reconfiguration of flexible plates in sheared flow. Mech. Res. Commun. 62, 1–4.

Heylen, W., Lammens, S., Sas, P., 1998. Modal analysis theory and testing. Katholieke Universiteit Leuven.

Huai, W.X., Zhang, J., Katul, G.G., Cheng, Y.G., Tang, X., Wang, W.J., 2019. The structure of turbulent flow through submerged flexible vegetation. J. Hydrodyn. 31, 1–19.

Huang, W.X., Shin, S.J., Sung, H.J., 2007. Simulation of flexible filaments in a uniform flow by the immersed boundary method. J. Comput. Phys. 226 (2), 2206–2228.

Huang, H.B., Wei, H., Lu, X.Y., 2017. Coupling performance of tandem flexible inverted flags in a uniform flow. J. Fluid Mech. 837, 461–476.

Jin, Y.Q., Kim, J.T., Chamorro, L.P., 2018a. Instability-driven frequency decoupling between structure dynamics and wake fluctuations. Phys. Rev. Fluids 3 (4), 044701.

Jin, Y.Q., Kim, J.T., Fu, S., Chamorro, L.P., 2019. Flow-induced motions of flexible plates: fluttering, twisting and orbital modes. J. Fluid Mech. 864, 273–285.

Jin, Y.Q., Kim, J.T., L., H., Chamorro, L.P., 2018b. Flow-induced oscillations of low-aspect-ratio flexible plates with various tip geometries. Phys. Fluids 30, 097102.

Jin, Y.Q., Kim, J.T., Mao, Z., Chamorro, L.P., 2018c. On the couple dynamics of wall-mounted flexible plates in tandem. J. Fluid Mech. 852, R2.

Kaneko, S., Nakamura, T., Inada, F., Kato, M., Ishihara, K., Nishihara, T., Mureithi, N.W., Langthjem, M.A., 2014. Flow-induced Vibrations: Classifications and Lessons from Practical Experiences, second ed. Elsevier Ltd..

Kim, D., Cossé, J., Cerdeira, C.H., Gharib, M., 2013. Flapping dynamics of an inverted flag. J. Fluid Mech. 736, R1.

Kim, S., Huang, W.X., Sung, H.J., 2010. Constructive and destructive interaction modes between two tandem flexible flags in viscous flow. J. Fluid Mech. 661, 511–521.

Leclercq, T., De Langre, E., 2016. Drag reduction by elastic reconfiguration of non-uniform beams in non-uniform flows. J. Fluids Struct. 60, 114–129.

Leclercq, T., De Langre, E., 2018. Reconfiguration of elastic blades in oscillatory flow. J. Fluid Mech. 838, 606–630.

Leclercq, T., Peake, N., De Langre, E., 2018. Does flutter prevent drag reduction by reconfiguration? Proc. R. Soc. A 474 (2209), 20170678.

Luhar, M., Nepf, H.M., 2011. Flow-induced reconfiguration of buoyant and flexible aquatic vegetation. Limnol. Oceanogr. 56, 2003–2017.

Luhar, M., Nepf, H.M., 2016. Wave-induced dynamics of flexible blades. J. Fluids Struct. 61, 20–41.

Nepf, H.M., 2012. Flow and transport in regions with aquatic vegetation. Annu. Rev. Fluid Mech. 44, 123–142.

Nové-Josserand, C., Hebrero, F.C., Petit, L.M., Megill, W.M., Godoy-Diana, R., Thiria, B., 2018. Surface wave energy absorption by a partially submerged bio-inspired canopy. Bioinspiration Biomim. 13 (3), 036006.

O'Connor, J., Revell, A., 2019. Dynamic interactions of multiple wall-mounted flexible flaps. J. Fluid Mech. 870, 189–216.

O'Connor, J., Revell, A., Mandal, P., Day, P., 2016. Application of a lattice boltzmann-immersed boundary method for fluid-filament dynamics and flow sensing. J. Biomech. 49, 2143–2151.

Peskin, C.S., McQueen, D.M., 1993. Computational biofluid dynamics. Contemp. Math. 143, 161–186.

Pinelli, A., Omidyeganeh, M., Brucker, C., Revell, A., Sarkar, A., Alinovi, E., 2016. The PELskin project: part IV - control of bluff body wakes using hairy filaments. Meccanica 52, 1503–1514.

Py, C., De Langre, E., Moulia, B., 2006. A frequency lock-in mechanism in the interaction between wind and crop canopies. J. Fluid Mech. 568, 425–449.

Ristroph, L., Zhang, J., 2008. Anomalous hydrodynamic drafting of interacting flapping flags. Phys. Rev. Lett. 101 (19), 194502.

Rockwell, D., Naudascher, E., 1978. Review of self-sustaining oscillations of flow past cavities. J. Fluids Eng. 100, 154–165.

Ryu, J., Park, S.G., Kim, B., Sung, H.J., 2015. Flapping dynamics of an inverted flag in a uniform flow. J. Fluids Struct. 57, 159–169.

Ryu, J., Park, S.G., Sung, H.J., 2018. Flapping dynamics of inverted flags in a side-by-side arrangement. Int. J. Heat Fluid Flow 70, 131–140.

Sader, J.E., Cossé, J., Kim, D., Fan, B., Gharib, M., 2016. Large-amplitude flapping of an inverted flag in a uniform steady flow–a vortex-induced vibration. J. Fluid Mech. 793, 524–555.

Saiidi, M., Douglas, B., Feng, S., 1994. Prestress force effect on vibration frequency of concrete bridges. J. Struct. Eng. 120, 2233–2241.

Shelley, M.J., Vandenberghe, N., Zhang, J., 2005. Heavy flags undergo spontaneous oscillations in flowing water. Phys. Rev. Lett. 94, 094302.

Shelley, M.J., Zhang, J., 2011. Flapping and bending bodies interacting with fluid flows. Annu. Rev. Fluid Mech. 43, 449–465.

Shoele, K., Mittal, R., 2016. Energy harvesting by flow-induced flutter in a simple model of an inverted piezoelectric flag. J. Fluid Mech. 790, 582–606.

Tao, J., Yu, X.B., 2012. Hair flow sensors: from bio-inspiration to bio-mimicking–a review. Smart Mater. Struct. 21, 113001.

Tian, F.B., Luo, H.X., Zhu, L.D., Lu, X.Y., 2011. Coupling modes of three filaments in side-by-side arrangement. Phys. Fluids 23, 111903.

Uddin, E., Huang, W.X., Sung, H.J., 2013. Interaction modes of multiple flexible flags in a uniform flow. J. Fluid Mech. 729, 563–583.
Wang, S.Z., He, G.W., Zhang, X., 2013. Parallel computing strategy for a flow solver based on immersed boundary method and discrete stream-function formulation. Comput. & Fluids 88, 210–224.
Wang, S.Z., Zhang, X., 2011. An immersed boundary method based on discrete stream function formulation for two-and three-dimensional incompressible flows. J. Comput. Phys. 230 (9), 3479–3499.
Yang, X., Liu, M., 2016. Bending modes and transition criteria for a flexible fiber in viscous flows. J. Hydrodyn. 28, 1043–1048.
Yu, Y.L., Liu, Y.Z., Amandolese, X., 2019. A review on fluid-induced flag vibrations. Appl. Mech. Rev. 71, 010801.
Zhang, J., Childress, S., Libchaber, A., Shelley, M.J., 2002. Flexible filaments in a flowing soap film as a model for one-dimensional flags in a two-dimensional wind. Nature 408, 835–839.
Zhu, L.D., 2007. Viscous flow past an elastic fibre tethered at its center point: vortex shedding. J. Fluid Mech. 587, 217–234.
Zhu, L.D., 2009. Interaction of two tandem deformable bodies in a viscous incompressible flow. J. Fluid Mech. 635, 455–475.
Zhu, X.J., He, G.W., Zhang, X., 2014a. How flexibility affects the wake symmetry properties of a self-propelled plunging foil. J. Fluid Mech. 751, 164–183.
Zhu, X.J., He, G.W., Zhang, X., 2014b. Numerical study on hydrodynamic effect of flexibility in a self-propelled plunging foil. Comput. & Fluids 97, 1–20.
Zhu, L.D., Peskin, C.S., 2002. Simulation of a flexible flapping filament in a flowing soap film by the immersed boundary method. J. Comput. Phys. 197, 452–468.
Zhu, L.D., Peskin, C.S., 2003. Interaction of two flapping filaments in a flowing soap film. Phys. Fluids 15, 1954–1960.